Chemical Mapping of Nano-defects within 2D Covalent Monolayers by Tip-enhanced Raman Spectroscopy

Feng Shao[1], Wenyang Dai[2], Yao Zhang[3], Wei Zhang[4], A. Dieter Schlüter[2*], Renato Zenobi[1*]

[1]*Department of Chemistry and Applied Biosciences, ETH Zurich, Vladimir-Prelog-Weg 3, CH-8093, Zurich, Switzerland*
[2]*Department of Materials, Institute of Polymers, ETH Zurich, Vladimir-Prelog-Weg 5, CH-8093, Zurich, Switzerland*
[3]*Center for Material Physics (CSIC - UPV/EHU and DIPC), Paseo Manuel de Lardizabal 5 Donostia 20018, Spain*
[4]*Department of Chemistry and Biochemistry, University of Colorado, Boulder, CO 80309, USA*

[*]*Corresponding authors: dieter.schluter@mat.ethz.ch; renato.zenobi@org.chem.ethz.ch*

Abstract

Nanoscale defects in monolayers (MLs) of two-dimensional (2D) materials, such as graphene, transition metal dichalcogenides (TMDCs), and 2D polymers (2DPs), can alter their physical, mechanical, optoelectronic, and chemical properties. However, detailed information about nano-defects within 2D covalent monolayers is difficult to obtain because it requires highly selective and sensitive techniques that can provide chemical information at the nanoscale. Here, we report a 2D imine-linked ML prepared from two custom-designed building blocks by dynamic imine chemistry at the air/water interface, in which an acetylenic moiety in one of the blocks was used as a spectroscopic reporter for nano-defects. Combined with density functional theory (DFT) calculations that take into account surface selection rules, tip-enhanced Raman spectroscopy (TERS) imaging provides information of the chemical bonds, molecular orientation, as well as nano-defects in the resulting ML. Additionally, TERS imaging visualizes the topography and integrity of the ML at Au(111) terrace edges, suggesting possible ductility of the ML. Furthermore, edge-induced molecular tilting and a stronger signal enhancement were observed at the terrace edges, from which a spatial resolution around 8 nm could be deduced. The present work can be used to study covalent 2D materials at the nanoscale, which are expected to be of use when engineering their properties for specific device applications.

KEYWORDS: *two-dimensional covalent monolayer, nano-defects, tip-enhanced Raman spectroscopy, dynamic imine chemistry, air/water interface, molecular orientation, acetylene unit*

Introduction

Nano-defects within monolayers (MLs) are able to significantly change many properties a 2D material would exhibit if it was structurally perfect. They can seriously weaken mechanical strength,[1,2] influence the band gap,[3] cause poor fracture characteristics,[4] and degrade the electronic performance, for example, of graphene.[5] Furthermore, they can act as undesirable sinks for charge carriers and electron–hole recombination centers through the Shockley–Read–Hall process in 2D metal dichalcogenides.[6] However, nano-defects can also induce magnetism in graphene,[7] increase grain boundary strength,[8] act as quasi-one-dimensional metallic wires,[9] and enhance the conductivity of graphene nanoribbons.[10,11] Moreover, they play pivotal roles in improving hydrogen evolution activity and determining the exciton dynamics of molybdenum disulfide monolayer.[12] Considered a structural analogue of graphene, 2D polymers (2DPs) are covalently linked monomolecular networks with periodic bonding and repeat units that exhibit long-range, in-plane order.[13-16] These organic 2D materials attracted intense attention in recent years due to their intriguing properties, which differ from those of their bulk counterparts.[15] With many applications in optoelectronics, catalysis, sensing, and as membranes,[17,18] 2DPs are especially interesting for polymer chemistry, surface engineering, and materials science.

Methods to observe and analyze nano-defects in 2D materials have relied mostly on microscopy tools, including transmission electron microscopy (TEM),[19,20] scanning tunneling microscopy (STM),[21] scanning transmission electron microscopy (STEM),[22] atomic force microscopy (AFM),[23] and optical microscopy (OM),[24] with a spatial resolution ranging from atomic to micrometer. However, these methods can only provide the morphology of the nano-defects without detailed chemical information. Although alternative approaches relying on Raman and photoluminescence spectroscopy can offer spectroscopic information about

defects,[25,26] they are restricted in their lateral resolution due to the diffraction limit of light. Compared to graphene, most synthetic 2DPs and related single sheets are poor heat conductors, and they can, for example, be instantaneously destroyed during TEM imaging. Thus, there is a real need for non-destructive and *in-situ* characterization techniques with high sensitivity and selectivity for nano-defects within covalent 2D materials.

Tip-enhanced Raman spectroscopy (TERS) offers an attractive solution for this challenge, as it integrates nanoscale spatial resolution of scanning probe microscopy (SPM) with the chemical selectivity of Raman spectroscopy, and can simultaneously provide topographic and molecular information of samples in a label-free fashion.[27-29] By means of field enhancement due to a combination of localized surface plasmon resonances and a lightning-rod effect at a metallic tip apex, TERS has shown single molecule sensitivity and down to sub-nanometer spatial resolution for experiments carried out on special samples at cryogenic temperatures.[30,31] In addition, TERS has been successfully used to visualize the nano-defect domains in MLs of graphene[10, 32-34] and TMDCs.[35,36] In a confocal Raman spectrum, all Raman-active modes can in principle be observed because these vibrational modes are averaged over all the molecules with random orientation.[31, 37,38] Conversely, a TER spectrum mainly shows the active modes of adsorbed molecules with a polarizability tensor in the direction of the tip axis. This selectivity of the Raman response can be viewed as a TERS surface selection rule on metallic substrates.[30,31,39,40] Selection rules thus enable TERS to access the orientation and configuration of molecules and of MLs deposited on conductive, flat surfaces.[40,41]

This contribution utilizes these rules to identify, quantify and localize nano-defects in a specially designed covalent monolayer sheet based on reversible imine chemistry.[15, 17, 42] For this purpose monomer **1** was designed (Fig. 1) which contains an acetylene unit, the Raman

and IR signal intensity of which is known to be particularly angle sensitive when it is adsorbed on a metal surface.[43-45] Also its Raman cross-section is attractively high and the signal assignment is unequivocal.[46] It is therefore a particularly attractive reporter although other changes in the TER spectra should not be ignored. In analogy to previous work,[15] the reaction between monomer **1** and the counter monomer **2** at an air/water interface was expected to result in a covalent polyimine network. All structural elements of this network were expected to lie flat while at the air/water interface and, more importantly, after transfer onto Au(111), a typical substrate used for TERS. It was anticipated that the acetylene unit of monomer **1** would be a perfect sensor for whether this monomer is integrated into a 2D network and, thus, is forced to lie flat on the metallic substrate or rather has degrees of conformational freedom which are obviously incompatible with a network structure and, thus, point towards defects. Thus, we expected to be able to identify defects of a polyimine network on a chemical basis just by the fact whether monomer **1** is TERS-silent or -active.

Here, we report the synthesis of a 2D covalent ML sheet from the two monomers 4-[2-(4-formylphenyl)ethynyl]benzaldehyde (**1**) and 1,3,5-trihexyl-2,4,6-tris(4-aminophenyl)-benzene (**2**, Fig.1a) at the air/water interface of a Langmuir-Blodgett (LB) trough. At first, these networks were investigated by OM, SEM, and AFM to confirm ML homogeneity. In a second step, several model compounds were prepared and analyzed by both confocal Raman and TER spectroscopy. In addition, an irregular 3D network of monomers **1** and **2** was investigated by confocal Raman. Moreover, TER spectra were also recorded from (sub-)MLs of the individual monomers **1** and **2**. With all this spectroscopic information at hand, and supported by the spectral predictions based on DFT calculations, the structure of the ML network synthesized from both monomers was established in terms of the imine bond.

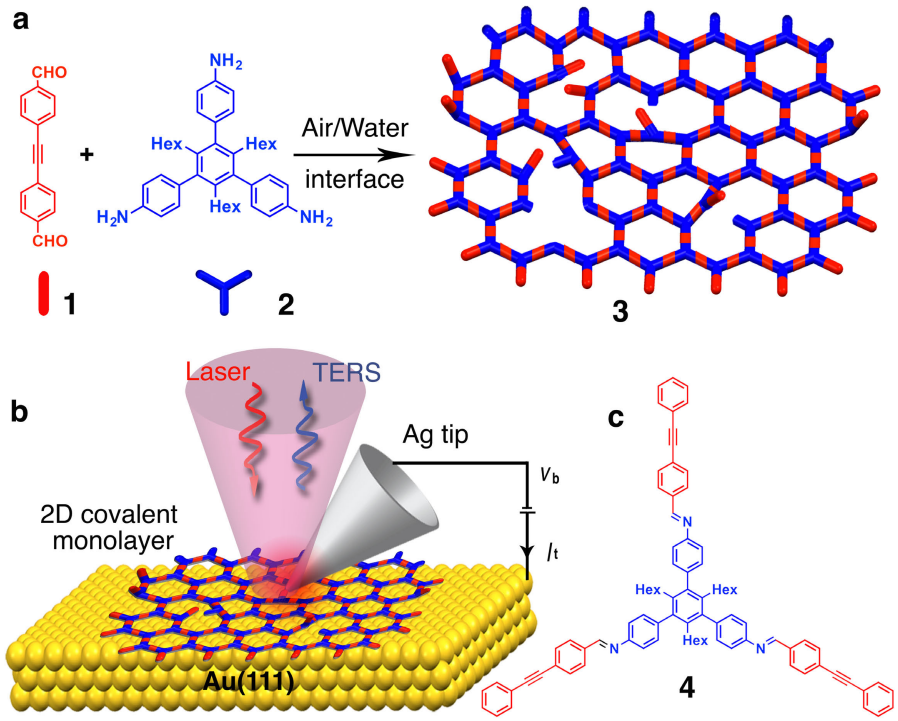

Figure 1. Synthesis and characterization of the 2D covalent monolayer sheet. (a) Synthesis of the monolayer sheet **3** with nano-defects from dialdehyde **1** and triamine **2**. (b) Schematic illustration of TERS experiment in a top-illumination configuration with the STM tunneling junction. (c) Chemical structure of the imine model compound **4**.

TERS mapping was performed next to unravel both defect frequency and lateral distribution of defects over a 100 × 100 nm^2 area of the same network with a resolution of 32 × 32 pixels (Fig. 1b). This was achieved mostly by measuring the acetylene signal intensity but also by considering other parts of the spectra. Furthermore, the acetylene TERS signal intensity can be used to provide information about how the covalent sheet of monomers **1** and **2** behaves when covering an atomic-scale Au(111) step edge of the underlying substrate. Would the sheet follow the shape of the step edge abruptly or more smoothly or would the sheet even rupture at the edge? These questions are qualitatively addressed by comparing the topography image of the substrate with the TERS image at the exact same position when the sheet covers the edge. Finally, the spatial resolution of the TER spectra recorded of the ML is determined at the substrate terrace steps.

Results and Discussion

The interfacial polymerization of monomers **1** and **2** was run overnight on a LB trough, while the surface pressure *versus* the mean molecular area (MMA) isotherm was recorded (Fig. S2). An imine-based ML, hereafter referred to as sheet **3**, was obtained at a surface pressure of 10 mNm^{-1}. At this pressure, the ML appeared homogeneous by Brewster angle microscopy (BAM, Fig. S3). The corresponding MMA was found to be 80 $Å^2$ (Fig. S2). By contrast, if the individual monomers **1** and **2** were compressed at the same surface pressure, crystalline domains and stripe/ribbon morphologies were observed (Fig. S3). Sheet **3** was vertically transferred onto both a silicon wafer and a TEM grid by the Schäfer technique.[15] OM of the sheet on the wafer proved it to be homogeneous (Fig. 2a) and on the TEM grid SEM imaging confirmed it to span holes up to a size of 160 × 160 μm^2 (Fig. 2b). This suggests high mechanical strength of sheet **3**, which if structurally perfect contains ~ 6×10^8 hexagonal pores (based on a pore size of 5.3 nm, Fig. S4), and indirectly confirms bond formation between the monomers. In contrast, the LB film of monomer **2** without the counter monomer having been present fails to span such holes under the same conditions (Fig. S5). Note that the three hydrophobic hexyl chains of monomer **2** render it a good candidate for interfacial polymerization because they effectively hinder crystallization of the monomer at the interface, which otherwise would occur (Fig. S6 and S7). Additionally, AFM imaging shows a continuous and smooth surface of the sheet with a thickness of ~ 0.84±0.05 nm (Fig. 2c, d and S8). Interestingly, the AFM profile of a ML of monomer **2** suggests approximately 0.2 nm of additional thickness (Fig. S9), which may stem from less ordered molecular orientations and tilting of the hexyl groups away from the surface.

To gain insight into the polymerization, confocal Raman spectra were recorded from the powders of monomers **1** and **2**, the irregular polyimine 3D network, and the imine model

compounds **4**, **5**, and **6** (Fig. S10 and S11), whereby model **4** is a finite size model for the irregular 3D network. All of the peak assignments were supported by DFT calculations (see Supportive Movies). The shoulder around 1,568 cm^{-1} (imine model **4**) can be assigned to the conjugated C=N stretching mode, proving the formation of imine bonds in the polyimine 3D network and the imine model compounds (Fig. S12). The presence of the imine bond in model compound **4** was further confirmed by nuclear magnetic resonance spectroscopy (NMR, Fig. S13-S15) and mass spectrometry (MS, Fig. S16).

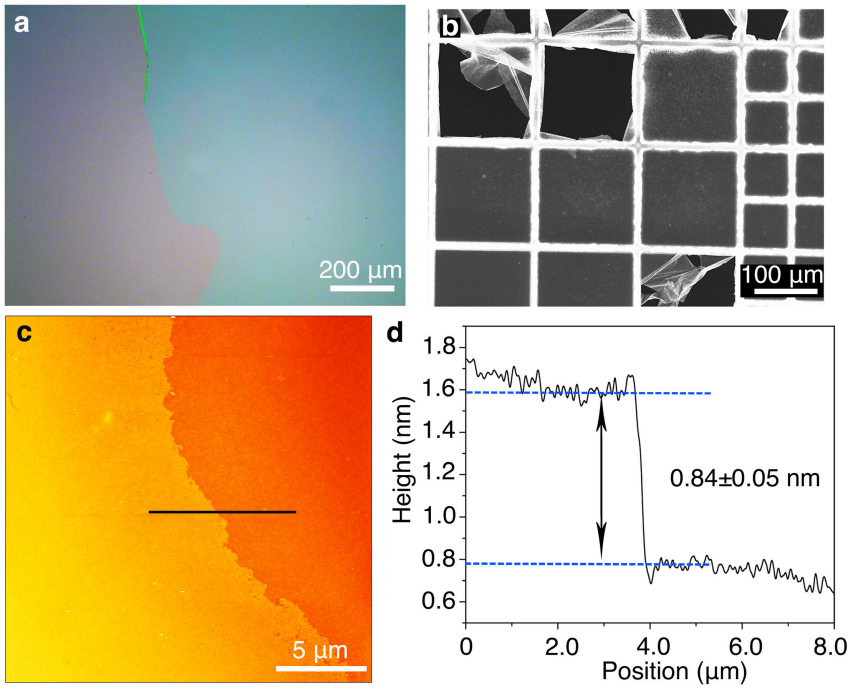

Figure 2. (a) Optical microscopy image of sheet **3** on SiO_2/Si substrate. (b) SEM image of the ML **3** suspended over a Cu grid. (c) AFM height image of sheet **3** on SiO_2/Si substrate. (d) Corresponding line profile along the black line in (c).

For a molecular dipole that is perpendicular to a conductive surface, the dipole moment will double due to image charges, whereas in a parallel orientation, the dipole moment will be canceled by its image charges. This is a surface selection rule for IR spectroscopy.[47,48] In TERS, assuming that the local field is mainly enhanced along the tip shaft (Z direction), the surface selection rules enable visualization of the vertical component of the Raman scattering tensor (α_{ZZ}) and thus of molecular orientation.[30,31] For studying the orientation, sub-MLs of

both monomers **1** and **2** on a clean Au(111) surface (Fig. S17) were prepared by spin-coating (0.4-0.5 ML, Fig. S18). Figs. 3a and 3e show typical TER spectra of these compounds as recorded from 100 × 100 nm^2 TERS maps, which were obtained with 32 × 32 pixels (Figs. 3b, 3f and S19). These spectra were recorded at the locations in the maps marked with numbers. The incidence of the corresponding colors are indicative of how frequently each type of spectrum occurs in the maps. Figures 3c, d, g, and h indicate the changes in the Raman tensor components $|\alpha_{ZZ}|^2$ of monomers **1** and **2** as the molecule rotates from a plane-parallel to a plane-perpendicular orientation with respect to the Au(111) surface (more details are shown in the Supporting Information). The fair agreement of the experimental data (Figs. 3a and 3e) with the calculated TERS spectra (Figs. 3c and 3g) suggests random adsorption of the monomers on the Au(111) surface. It is worth noting that the simulation of the TERS spectra in the present work is based on a simplified Raman tensor model without considering intermolecular and molecule-substrate interactions.[30,31]

According to the calculations (Figs. S20-22), the vibrational modes at 2,220 cm^{-1} for monomer **1** and at 1,180 cm^{-1} for monomer **2**, as well as the modes around 1,600 cm^{-1} of both compounds are orientation-dependent. Because enhancement in TERS vary with laser power and tip-sample distance,[27] TERS intensity ratio maps were evaluated to assess the molecular orientation distribution of the sub-MLs, as shown in Figs. 3b and 3f, respectively. Significant orientation fluctuations are found in the TER spectra located in different pixels and in the intensity ratio maps of the individual monomers on the Au(111) surface (Fig. 3). This is because the TERS spectral profile is sensitive to the adsorption configuration and orientation on the Au surface.[31, 40]

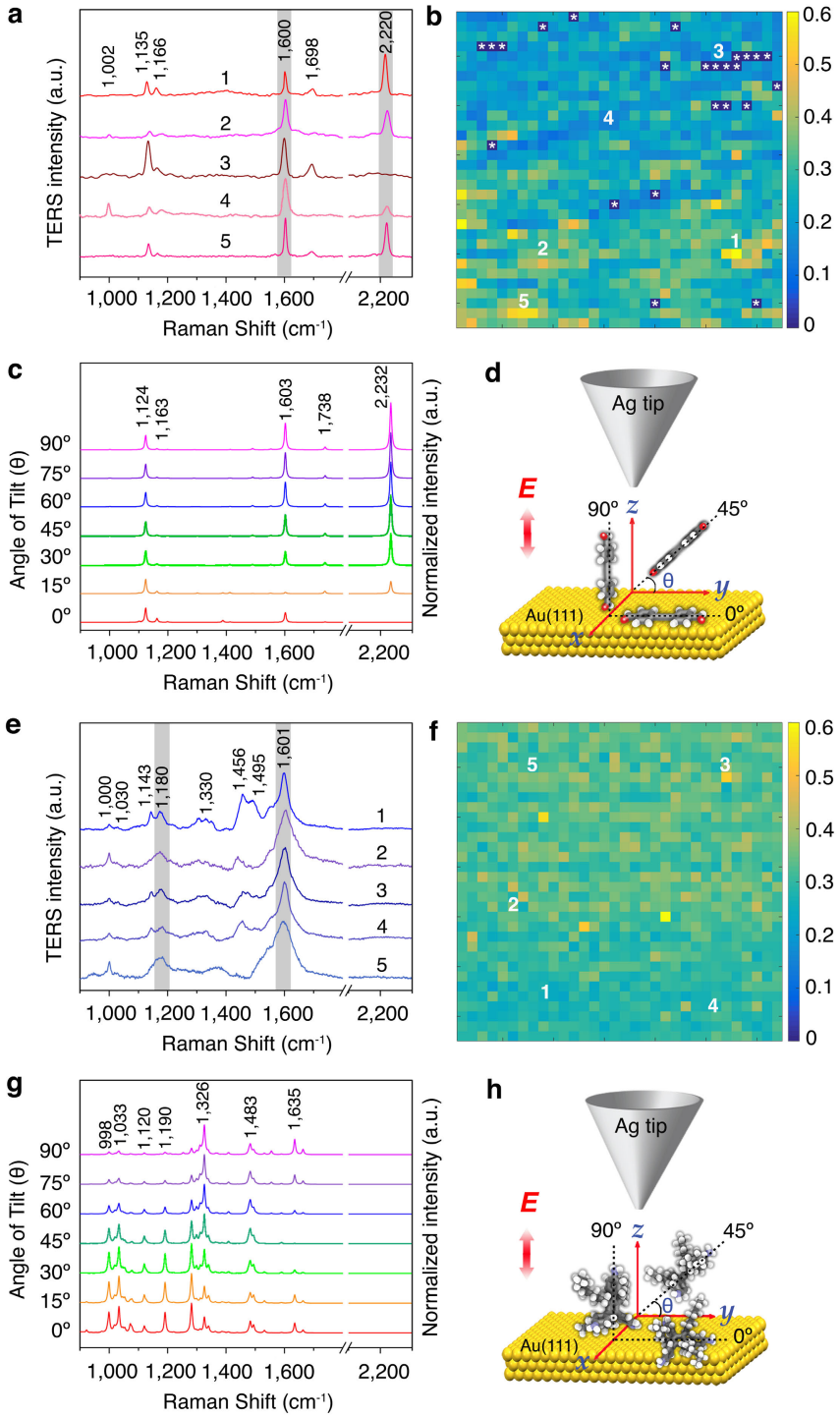

Figure 3. Experimental and calculated TER spectra of monomers. Typical experimental (a, e) and calculated (c, g) TER spectra of monomer **1** and monomer **2**, respectively. (a, e, and g) are normalized to the highest peak, (c) is normalized to the 1,124 cm^{-1} band. The spectra in (a, c) were recorded at the locations marked in the maps. (b, f) TERS intensity ratio imaging of monomer **1** ($I_{2,220}$ to $I_{1,600}$) and monomer **2** ($I_{1,180}$ to $I_{1,600}$) indicate different molecular orientation distributions. The dark blue pixels with a white star in (b) are locations where the triple bond in monomer **1** is parallel to the Au(111) surface. All the maps were measured over a 100×100 nm^2 area with 32×32 pixels on the substrate. (d, h) Schematics of the plane-parallel and plane-perpendicular orientations, respectively. Only the vertical compound of the local field E is considered for field enhancements. The molecular bending and twisting angles are held constant at 0°.

In order to further study the orientation, more TERS spectra of monomer **1** were calculated. We gradually rotated the molecular plane while keeping the molecular axis parallel to the surface (Fig. S23), or fixing the molecular axis with a small angle (15º, Fig. S24) with respect to Au(111). In addition, we also compared *cis* (Fig. 3) with *trans* (Fig. S25) isomers of monomer **1**. Indeed, even a small change in either orientation of the molecular plane or angle of the symmetry axis (*e.g.*, 5º and 10º, Fig. S21) with respect to the surface can considerably influence the relative peak intensities. Especially, the band at 2,232 cm^{-1} (C≡C stretching vibration, see Movie S1) will be absent only when the triple bond is parallel to the Au(111) surface because it only changes polarizability in XY plane, confirming that it can act as an orientation indicator for the 2D network. Notably, due to thermal diffusion and motion under ambient conditions, a variety of adsorption geometries and molecular orientations contribute to the TER spectra. Consequently, these simulations cannot provide information to calculate accurate values of the molecular tilt angle, but can be used to statistically estimate the molecular configuration which is flat-lying or tilt-up with respect to the metal surface.[40, 49] The probability of monomer **1** lying flat on the Au(111) surface is approximately 2.5% at ambient temperature, as indicated by the dark blue pixels marked with a white star in Fig. 3b and Fig. S26. In other words, most monomers **1** tend to tilt up on the surface when spin-coating was used for sample preparation. Even though some errors, *e.g.*, temporary loss in the STM feedback, random adsorption of contaminations on the tip apex, and a weak TERS response during part of the image acquisition, cannot be completely excluded, this was not the case for the dark blue pixesl in Fig. 3b: usable TERS data could still be extracted from all these location, however there was no observable signal of the triple bond (2,220 cm^{-1}; spectrum 3 in Fig. 3a) in these pixels.

Next, we investigated the molecular orientation of the triple bonds within sheet **3**, a sub-ML of a mixture of both monomers, and a sub-ML of imine model compound **4** (Fig. 4).

TERS signal-to-noise ratio (S/N) maps (100 × 100 nm^2, 32 × 32 pixels) at 2,220 cm^{-1} are reported in Fig. 4. The map in Fig. 4a is characterized by a homogeneous S/N distribution, with only ~ 2% pixels (red) having S/N⩾3. In other words, sheet **3** contains very few of the triple bonds not lying flat on Au(111). This suggests that almost all of them (~ 98%) are "locked" into the 2D network. Conversely, under the same conditions, only ~ 2.5% triple bonds in the sub-ML of monomer **1** appear to lie flat on the surface (Fig. 3b). Accordingly, one can make the assumption that red pixels in Fig. 4a (S/N⩾3) represent nano-defects within sheet **3**, in which the imine bonds have broken or were not formed at all and segments containing triple bonds tilt away from the plane of the 2D network (Fig. 4f). This phenomenon is also reproduced for the same sheet deposited on a template-stripped Au surface, where ~3% nano-defects are observed (Fig. S27). However, these values also have to be considered with care as there may be abovementioned artifacts in Fig. 3.

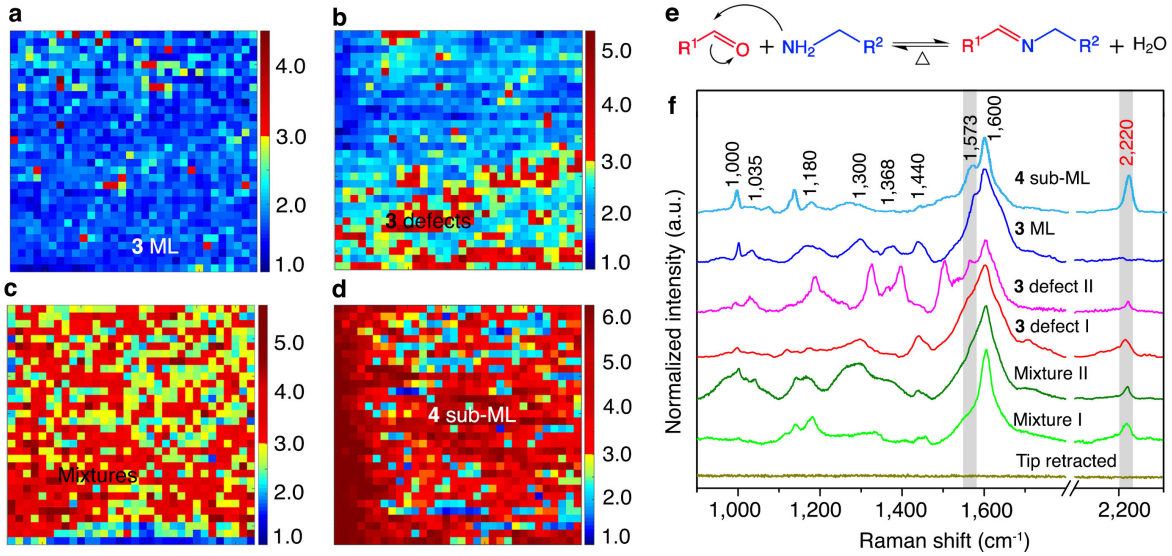

Figure 4. TERS imaging and spectra of the 2D covalent monolayer. (a) TERS signal-to-noise ratio imaging of the triple bond at 2,220 cm^{-1} within the intact sheet **3**, and, (b), within the broken monolayer sheet **3** after heating under water at 70 °C for 30 min. (c, d) TERS signal-to-noise ratio imaging of the triple bond at 2,220 cm^{-1} within the sub-monolayers prepared from (c) a mixed solution of monomer **1** and monomer **2** with the molar ratio of 1:3, and (d) imine model **4** by spin-coating. All the maps were measured over a 100×100 nm^2 area with 32×32 pixels on the Au(111) surface. (e) Reversible processes associated with imine chemistry. The equilibrium of imine formation obtained through intermediate hemiaminal formation. (f) Representative TER spectra obtained from different maps.

Several lines of experimental evidence were obtained to support this hypothesis. First of all, after half an hour heating under water at 70 °C, in all areas sampled more nano-defects (~20%) within the imine-linked ML can be observed due to the reversibility of imine bond formation (Figs. 4b, e). Furthermore, the triple bonds within the sub-ML of mixed monomers and imine model compound **4** hardly lie flat (<10%) on the surface (Figs. 4c, d). This is similar to the situation of the sub-ML of monomer **1** (~ 2.5%, Fig. 3b). Further supporting evidence is provided by the TER spectra of nano-defects in the intact and broken covalent ML, the sub-ML of mixed monomers, and the sub-ML of imine model compound **4** (Fig. 4f). The fact that the imine bond vibraton at 1,573 cm^{-1} is sometimes still visible in defect areas originates from the fact that the defect itself can be significantly smaller than the area "seen" by the TERS tip. Several important observations can be made. First, the TER spectrum acquired from sheet **3** is different from the corresponding Raman spectrum of the corresponding 3D polyimine powder (Fig. 5), suggesting that TERS mainly visualizes the Raman vibrational modes containing out-of-plane components. Second, compared to the sub-ML of mixed monomers without polymerization, the presence of a significant band around 1,573 cm^{-1} and higher full width at half maximum (FWHM) of the band around 1,600 cm^{-1} indicate the formation of imine bonds in the TER spectra of the nano-defects (Fig. S28 and 29). Finally, apart from the triple bond, the TER spectra of the nano-defects also show some fingerprints of the 2D covalent ML (**3** defect I, Fig. 4f) or the monomer **2** sub-ML (**3** defect II, Fig. 4f), suggesting they partly contain similar chemical structures.

It should also be pointed out that when sheet **3** covers terrace steps on Au(111), the edges can induce a tilted orientation and stronger signal enhancement than that on plane sites (Fig. 5). A TERS S/N map (100 × 100 nm^2) at 2,220 cm^{-1} (Fig. 5a) and an intensity map at 1,600 cm^{-1} (Fig. 5b) were obtained at an atomic step edge (Fig. 5e). It is worth noting that in order

to avoid the sheet from being scratched, a low tunneling current (0.1V, 0.1nA) was applied for TERS mapping, while a high current (0.1V, 1.0 nA) was used for STM imaging at the same area (Fig. 5f and S30). Obviously, the triple bond contained in the sheet artificially tilts at the edge in terms of the S/N⩾3 criterion at 2,220 cm^{-1} (Fig. 5a and S30).

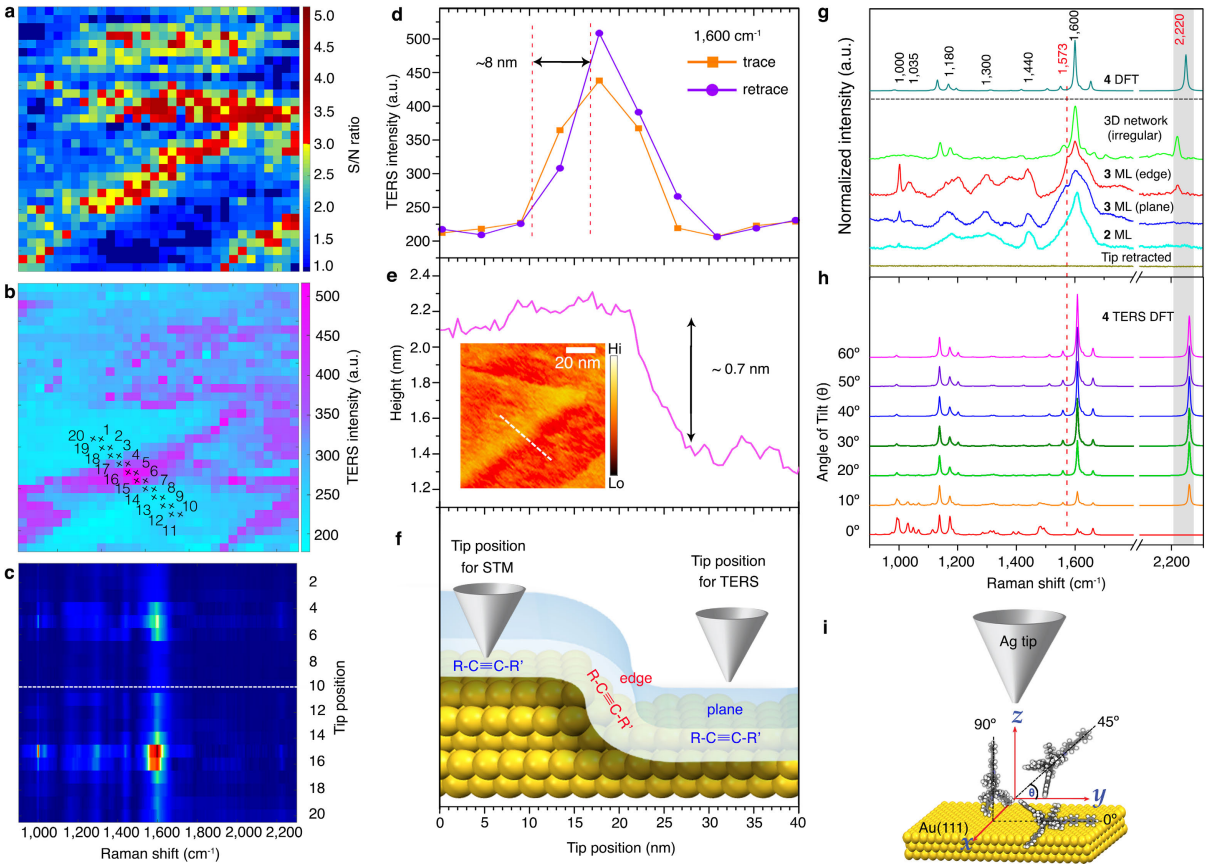

Figure 5. TERS imaging of edge-induced molecular tilt within the 2D covalent monolayer. (a) TERS signal-to-noise ratio image at 2,220 cm^{-1} and, (b) TERS intensity image at 1,600 cm^{-1} of the monolayer on a terrace of the Au(111) substrate. The maps were measured over a 100 × 100 nm^2 area with 32× 32 pixels. (c) Color-coded intensity map of two line-trace TERS scans taken in (b). (d) Corresponding TERS intensity of the band at 1,600 cm^{-1} along the trace and retrace scans. The spatial resolution is estimated to be around 8 nm using a 10-90% contrast criterion. (e) STM image and corresponding topographic height profile of the terrace after TERS imaging. (f) Schematic of edge-induced molecular tilt within the monolayer. STM image (0.2V, 1.0 nA) taken after TERS maps (0.2 V, 0.1 nA) with different parameters to avoid scratching the monolayer. (g) TER spectra recorded from the monolayer on the plane and edge positions of Au(111) substrate. (h) Calculated TER spectra of imine model **4**, normalized to the 1,124 cm^{-1} band. (i) Schematics of the plane-parallel configuration and plane-perpendicular configuration, respectively. The molecular bending and twisting angles are held constant at 0°.

Additionally, the edge can also produce stronger TERS intensities (1,600 cm^{-1}) than that on flat surface sites (Fig. 5b). Indeed, previous theoretical calculations predicted that a stronger localization of the electromagnetic field and thus a higher TERS intensity can be observed at

atomic steps due to lighting-rod and plasmonic effects.[50,51] Moreover, the color-coded map indicates the variation of the TERS intensity with trace and retrace scans at 1,600 cm^{-1}, offering obvious contrasts between edges and flat surfaces (Fig. 5c and S31). Furthermore, the line profile analysis suggests a spatial resolution of ~8 nm, using the 10-90% criterion (Fig. 5d) or the full-width at half-maximum (Fig. S32) at the edges. However, the real spatial resolution may in fact be underestimated because the setup is subject to thermal drift and experimental artefacts under ambient conditions (Fig. S33).[29, 52]

When comparing the STM topography image of the Au(111) substrate (Fig. 5e, inset) with the TERS intensity image (Fig. 5b) of the same area, a different lateral resolution of the STM image (~5 nm) and the TERS map (~8 nm) was obtained. This is simply due to the lower number of pixels in the TERS map, but also to a larger tip-to-sample distance to avoid any scratching. The resolution of the STM image may be blurred because sharp edges of the Au(111) that are covered by sheet **3** appear smoothed (Fig. 5f). However, compared to the ML of monomer **2**, the imine bond vibrational mode around 1,573 cm^{-1} can be observed in the TER spectra of sheet **3** at both plane and edge sites (Fig. 5g). Additionally, besides the triple bond vibrational mode at 2,220 cm^{-1} (Fig. 5g), there are no significant bands characteristic of nano-defects (*e.g.*, peaks in the 1,000-1,500 cm^{-1} fingerprint region) that can be observed from sheet **3** deposited on the edges. Hence, this evidence indicates that sheet **3** prefers a tilted orientation as opposed to nano-defects or rupture at the edges, possibly due to ductility of the imine-linked soft sheet. This is also fully supported by the results of the DFT calculations (Fig. 5h and 5i).

Conclusions

In summary, we reported the synthesis and characterization of a 2D covalent sheet **3**, in which the nano-defects can be identified, quantified, and localized by TERS imaging. The

large-size, transferrable, imine-linked ML with a thickness of ~0.8 nm was prepared through dynamic imine chemistry at the air/water interface. The formation of imine bonds within the 2D network was confirmed by comparing it to several imine model compounds, whose identity was also confirmed by confocal Raman spectroscopy and TERS imaging. Supported by DFT calculations that take surface selection rules into consideration, TERS can provide chemical information about the end groups used, newly formed imine bonds, molecular orientation, and nano-defects in the resulting ML with a spatial resolution around 8 nm. Importantly, by introducing a triple bond as a spectroscopic reporter group, we find that the 2D covalent ML lies flat on the Au(111) surface, with a homogeneous orientation distribution locked by the imine network. ~3% nano-defect domains are observed and localized in the network where imine bonds have broken or were not formed at all, and the residual segments containing the triple bond tend to tilt up. However, the triple bonds in a sub-ML of mixed monomers and imine model compound **4** hardly lie flat (<10%) on the Au(111) surface when an imine-linked network is absent. Additionally, TERS imaging visualizes the topography and integrity of the ML sheet at the Au(111) terrace steps, in which the ML smoothly covers the edge and thus will cause the orientation tilt instead of the nano-defects or rupture. The presented methodology can be generally applied to nanoscale chemical analysis of covalent 2D materials, thereby promoting their application in electronic or optoelectronic devices.

Methods

Synthesis of 2D covalent monolayer. The 2D covalent ML was prepared on a Langmuir–Blodgett trough (KSV 2000 System 2, KSV NIMA, Finland). The trough was filled with ultrapure water (Mill-Q, Millipore, 18.2 MΩ cm resistivity) and placed on an anti-vibration table in a dust-reduced environment. The surface pressure was measured with a Wilhelmy balance with a precision of 0.01 mN m^{-1}. A typical experiment proceeded as follows: 25 μL

of a 1.0 mg mL^{-1} solution of monomer **1** was pre-mixed with 75 μL of a 1.0 mg mL^{-1} solution of monomer **2** in $CHCl_3$. The resulting solution (50 μL) was spread on the air/water interface with a microliter syringe. The solvent was allowed to evaporate for 30 min, afterwards the compression was carried out at a rate of 3 mm min^{-1} until the surface pressure stabilized at 10 mN m^{-1}. Trifluoroacetic acid (0.35 mL) was then added dropwise into the solution without disturbing the interfacial monolayer. After overnight polymerization at 10 mN m^{-1}, a pre-submerged substrate (silicon wafer or Au(111) substrate) was pulled up at a constant rate of 0.5 mm min^{-1}. After drying at room temperature, the collected ML was subjected to optical microscopy, SEM, AFM and TERS measurements. Dilute solutions of monomers and imine models in chloroform (~25 μM) were used for spin-coating. In order to get sub-ML samples, a 50 μL portion of the diluted solutions were placed on the Au(111) substrate, which was spun at 2500 rpm.[53]

TERS measurements. All TERS and confocal Raman spectra were acquired on a combined STM/Raman microscope (Ntegra Spectra, NT-MDT, Zelenograd, Russia) which was enclosed by a home-made acoustic isolation box and operated under ambient conditions. The instrument is equipped with an air objective (100×, NA=0.7, Mitutoyo, Japan) and an electron multiplying charge-coupled device (EMCCD, Newton 971 UVB, Andor, Belfast, UK). The spectrometer was calibrated by a standard Neon lamp (Renishaw, UK). TERS probes were prepared by electrochemical etching of a silver wire (diameter 0.25 mm, 99.9985% purity, Alfa Aesar). A 3:1 (v/v) mixture of ethanol (absolute, Sigma-Aldrich) and perchloric acid (70%, Sigma-Aldrich) was used as etchant. A potential of 8 V was applied and a current of ≈10 mA was measured during the etching process. TERS maps were collected in STM feedback (constant current mode) with the sample surface be moved by the piezo sample stage in the x, y, and z directions while keeping the relative laser-to-tip position fixed. The

dynamic range of the piezo scanner (6.0 μm × 6.0 μm in XY and 2.0 μm in Z with 220 V) is small, which ensures highly precise control of the tip-substrate gap and XY coordinate with a < 0.1 nm step size. An exposure time of 5 s and 2 accumulations were used for all spectra. A 632.8 nm HeNe laser at an incident power of 0.5 mW was used as the excitation source. During TERS measurements, the bias voltage was set to 0.2 V and the tunneling current was kept at 0.1 nA to avoid scratching the sheet. All TERS images were obtained after overnight measurements (continuous laser illumination and data recording) to minimize the thermal drift of the system. In order to get better STM imaging, the bias voltage at 0.2 V and tunneling current at 1.0 nA were applied after TERS mapping. Spectral processing followed previously described procedures.[40]

Supporting Information

Experimental details, materials and model compounds, DFT TERS calculations, and supporting vibrational movies. Analytical data includes BAM, AFM, STM, ^{1}H, ^{13}C-NMR, MALDI-TOF-MS, confocal Raman spectroscopy analysis. The supporting information is available free of charge on the ACS publication website.

Acknowledgements

We thank the ETH Zürich for financial support. F.S. thanks the Chinese Scholarship Council for a Ph.D. student fellowship. We thank Dr. Christian Wäckerlin (EMPA, Switzerland) for the help in sputtering clean of the Au(111) substrates and Eunice Phua (The University of Tokyo) for the preparation of LB films.

References

1. Lee, S.-M.; Kim, J.-H.; Ahn, J.-H., Graphene as a Flexible Electronic Material: Mechanical Limitations by Defect Formation and Efforts to Overcome. *Mater. Today* **2015,** *18*, 336-344.

2. Zandiatashbar, A.; Lee, G.-H.; An, S. J.; Lee, S.; Mathew, N.; Terrones, M.; Hayashi, T.; Picu, C. R.; Hone, J.; Koratkar, N., Effect of Defects on the Intrinsic Strength and Stiffness of Graphene. *Nat. Commun.* **2014,** *5*.
3. Pandey, M.; Rasmussen, F. A.; Kuhar, K.; Olsen, T.; Jacobsen, K. W.; Thygesen, K. S., Defect-Tolerant Monolayer Transition Metal Dichalcogenides. *Nano Lett.* **2016,** *16*, 2234-2239.
4. Hwangbo, Y.; Lee, C.-K.; Kim, S.-M.; Kim, J.-H.; Kim, K.-S.; Jang, B.; Lee, H.-J.; Lee, S.-K.; Kim, S.-S.; Ahn, J.-H., Fracture Characteristics of Monolayer CVD-graphene. *Sci. Rep.* **2014,** *4*.
5. Schwierz, F., Graphene Transistors. *Nat. Nanotechnol.* **2010,** *5* (7), 487-496.
6. Liu, Y.; Xu, F.; Zhang, Z.; Penev, E. S.; Yakobson, B. I., Two-Dimensional Mono-Elemental Semiconductor with Electronically Inactive Defects: The Case of Phosphorus. *Nano Lett.* **2014,** *14*, 6782-6786.
7. Yazyev, O. V.; Helm, L., Defect-induced Magnetism in Graphene. *Phys. Rev. B* **2007,** *75*, 125408.
8. Wei, Y.; Wu, J.; Yin, H.; Shi, X.; Yang, R.; Dresselhaus, M., The Nature of Strength Enhancement and Weakening by Pentagon–heptagon Defects in Graphene. *Nat. Mater.* **2012,** *11*, 759-763.
9. Lahiri, J.; Lin, Y.; Bozkurt, P.; Oleynik, I. I.; Batzill, M., An Extended Defect in Graphene as a Metallic Wire. *Nat. Nanotechnol.* **2010,** *5*, 326-329.
10. Stadler, J.; Schmid, T.; Zenobi, R., Nanoscale Chemical Imaging of Single-Layer Graphene. *ACS Nano* **2011,** *5*, 8442-8448.
11. Banhart, F.; Kotakoski, J.; Krasheninnikov, A. V., Structural Defects in Graphene. *ACS Nano* **2011,** *5*, 26-41.
12. Ye, G.; Gong, Y.; Lin, J.; Li, B.; He, Y.; Pantelides, S. T.; Zhou, W.; Vajtai, R.; Ajayan, P. M., Defects Engineered Monolayer MoS2 for Improved Hydrogen Evolution Reaction. *Nano Lett.* **2016,** *16*, 1097-1103.
13. Schlüter, A. D.; Payamyar, P.; Öttinger, H. C., How the World Changes By Going from One- to Two-Dimensional Polymers in Solution. *Macromol. Rapid Comm.* **2016,** *37*, 1638-1650.
14. Payamyar, P.; King, B. T.; Ottinger, H. C.; Schluter, A. D., Two-dimensional Polymers: Concepts and Perspectives. *Chem. Comm.* **2016,** *52*, 18-34.
15. Dai, W.; Shao, F.; Szczerbiński, J.; McCaffrey, R.; Zenobi, R.; Jin, Y.; Schlüter, A. D.; Zhang, W., Synthesis of a Two-Dimensional Covalent Organic Monolayer through Dynamic Imine Chemistry at the Air/Water Interface. *Angew. Chem. Int. Ed.* **2016,** *55*, 213-217.
16. Sakamoto, J.; van Heijst, J.; Lukin, O.; Schlüter, A. D., Two-Dimensional Polymers: Just a Dream of Synthetic Chemists? *Angew. Chem. Int. Ed.* **2009,** *48*, 1030-1069.
17. Sahabudeen, H.; Qi, H.; Glatz, B. A.; Tranca, D.; Dong, R.; Hou, Y.; Zhang, T.; Kuttner, C.; Lehnert, T.; Seifert, G.; Kaiser, U.; Fery, A.; Zheng, Z.; Feng, X., Wafer-sized Multifunctional Polyimine-based Two-dimensional Conjugated Polymers with High Mechanical Stiffness. *Nat. Commun.* **2016,** *7*, 13461.
18. Boott, C. E.; Nazemi, A.; Manners, I., Synthetic Covalent and Non-Covalent 2D Materials. *Angew. Chem. Int. Ed.* **2015,** *54*, 13876-13894.

19. Hashimoto, A.; Suenaga, K.; Gloter, A.; Urita, K.; Iijima, S., Direct evidence for atomic defects in graphene layers. *Nature* **2004,** *430*, 870-873.

20. Fan, Y.; Goldsmith, B. R.; Collins, P. G., Identifying and Counting Point Defects in Carbon Nanotubes. *Nat. Mater.* **2005,** *4*, 906-911.

21. Tapasztó, L.; Nemes-Incze, P.; Dobrik, G.; Jae Yoo, K.; Hwang, C.; Biró, L. P., Mapping the Electronic Properties of Individual Graphene Grain Boundaries. *Appl. Phys. Lett.* **2012,** *100*, 053114.

22. Huang, P. Y.; Ruiz-Vargas, C. S.; van der Zande, A. M.; Whitney, W. S.; Levendorf, M. P.; Kevek, J. W.; Garg, S.; Alden, J. S.; Hustedt, C. J.; Zhu, Y.; Park, J.; McEuen, P. L.; Muller, D. A., Grains and Grain Boundaries in Single-layer Graphene Atomic Patchwork Quilts. *Nature* **2011,** *469*, 389-392.

23. Nemes-Incze, P.; Yoo, K. J.; Tapasztó, L.; Dobrik, G.; Lábár, J.; Horváth, Z. E.; Hwang, C.; Biró, L. P., Revealing the Grain Structure of Graphene Grown by Chemical Vapor Deposition. *Appl. Phys. Lett.* **2011,** *99*, 023104.

24. Duong, D. L.; Han, G. H.; Lee, S. M.; Gunes, F.; Kim, E. S.; Kim, S. T.; Kim, H.; Ta, Q. H.; So, K. P.; Yoon, S. J.; Chae, S. J.; Jo, Y. W.; Park, M. H.; Chae, S. H.; Lim, S. C.; Choi, J. Y.; Lee, Y. H., Probing Graphene Grain Boundaries with Optical Microscopy. *Nature* **2012,** *490*, 235-239.

25. Ferrari, A. C.; Meyer, J. C.; Scardaci, V.; Casiraghi, C.; Lazzeri, M.; Mauri, F.; Piscanec, S.; Jiang, D.; Novoselov, K. S.; Roth, S.; Geim, A. K., Raman Spectrum of Graphene and Graphene Layers. *Phys. Rev. Lett.* **2006,** *97*, 187401.

26. Schwarz, S.; Kozikov, A.; Withers, F.; Maguire, J. K.; Foster, A. P.; Dufferwiel, S.; Hague, L.; Makhonin, M. N.; Wilson, L. R.; Geim, A. K.; Novoselov, K. S.; Tartakovskii, A. I., Electrically Pumped Single-defect Light Emitters in WSe_2. *2D Mater.* **2016,** *3*, 025038.

27. Schmid, T.; Opilik, L.; Blum, C.; Zenobi, R., Nanoscale Chemical Imaging Using Tip-Enhanced Raman Spectroscopy: A Critical Review. *Angew. Chem. Int. Ed.* **2013,** *52*, 5940-5954.

28. Wang, X.; Huang, S.-C.; Huang, T.-X.; Su, H.-S.; Zhong, J.-H.; Zeng, Z.-C.; Li, M.-H.; Ren, B., Tip-enhanced Raman Spectroscopy for Surfaces and Interfaces. *Chem. Soc. Rev.* **2017,** *46*, 4020-4041.

29. Richard-Lacroix, M.; Zhang, Y.; Dong, Z.; Deckert, V., Mastering High Resolution Tip-enhanced Raman Spectroscopy: Towards a Shift of Perception. *Chem. Soc. Rev.* **2017,** *46*, 3922-3944.

30. Zhang, R.; Zhang, Y.; Dong, Z.; Jiang, S.; Zhang, C.; Chen, L.; Zhang, L.; Liao, Y.; Aizpurua, J.; Luo, Y., Chemical Mapping of a Single Molecule by Plasmon-enhanced Raman Scattering. *Nature* **2013,** *498*, 82-86.

31. Jiang, S.; Zhang, Y.; Zhang, R.; Hu, C.; Liao, M.; Luo, Y.; Yang, J.; Dong, Z.; Hou, J. G., Distinguishing Adjacent Molecules on a Surface Using Plasmon-enhanced Raman Scattering. *Nat. Nanotechnol.* **2015,** *10*, 865-869.

32. Wang, P.; Zhang, D.; Li, L.; Li, Z.; Zhang, L.; Fang, Y., Reversible Defect in Graphene Investigated by Tip-Enhanced Raman Spectroscopy. *Plasmonics* **2012,** *7*, 555-561.

33. Rickman, R.; Dunstan, P., Enhancement of Lattice Defect Signatures in Graphene and Ultrathin Graphite Using Tip-enhanced Raman Spectroscopy. *J. Raman Spectrosc.* **2014,** *45*, 15-21.

34. Li, X.; Liu, Y.; Zeng, Z.; Wang, P.; Fang, Y.; Zhang, L., Investigation on Tip Enhanced Raman Spectra of Graphene. *Spectrochim. Acta A* **2018,** *190*, 378-382.

35. Rahaman, M.; Rodriguez, R. D.; Plechinger, G.; Moras, S.; Schüller, C.; Korn, T.; Zahn, D. R. T., Highly Localized Strain in a MoS_2/Au Heterostructure Revealed by Tip-Enhanced Raman Spectroscopy. *Nano Lett.* **2017,** *17*, 6027-6033.

36. Park, K.-D.; Khatib, O.; Kravtsov, V.; Clark, G.; Xu, X.; Raschke, M. B., Hybrid Tip-Enhanced Nanospectroscopy and Nanoimaging of Monolayer WSe_2 with Local Strain Control. *Nano Lett.* **2016,** *16*, 2621-2627.

37. Sun, M.; Fang, Y.; Zhang, Z.; Xu, H., Activated Vibrational Modes and Fermi Resonance in Tip-enhanced Raman Spectroscopy. *Phys. Rev. E* **2013,** *87*, 020401.

38. Watanabe, H.; Hayazawa, N.; Inouye, Y.; Kawata, S., DFT Vibrational Calculations of Rhodamine 6G Adsorbed on Silver: Analysis of Tip-Enhanced Raman Spectroscopy. *J. Phys. Chem. B* **2005,** *109*, 5012-5020.

39. Jiang, N.; Chiang, N.; Madison, L. R.; Pozzi, E. A.; Wasielewski, M. R.; Seideman, T.; Ratner, M. A.; Hersam, M. C.; Schatz, G. C.; Van Duyne, R. P., Nanoscale Chemical Imaging of a Dynamic Molecular Phase Boundary with Ultrahigh Vacuum Tip-Enhanced Raman Spectroscopy. *Nano Lett.* **2016,** *16*, 3898-3904.

40. Shao, F.; Müller, V.; Zhang, Y.; Schlüter, A. D.; Zenobi, R., Nanoscale Chemical Imaging of Interfacial Monolayers by Tip-Enhanced Raman Spectroscopy. *Angew. Chem. Int. Ed.* **2017,** *56*, 9361-9366.

41. Berweger, S.; Neacsu, C. C.; Mao, Y.; Zhou, H.; Wong, S. S.; Raschke, M. B., Optical Nanocrystallography with Tip-enhanced Phonon Raman Spectroscopy. *Nat. Nanotechnol.* **2009,** *4*, 496-499.

42. Jin, Y.; Wang, Q.; Taynton, P.; Zhang, W., Dynamic Covalent Chemistry Approaches Toward Macrocycles, Molecular Cages, and Polymers. *Acc. Chem. Res.* **2014,** *47*, 1575-1586.

43. Millen, R. P.; de Faria, D. L. A.; Temperini, M. L. A., Vibrational Spectra of 2-ethynylpyridine and Its Silver Salt. *Vib. Spectrosc.* **2001,** *27*, 89-96.

44. Joo, S.-W.; Kim, K., Adsorption of Phenylacetylene on Gold Nanoparticle Surfaces Investigated by Surface-enhanced Raman Scattering. *J. Raman Spectrosc.* **2004,** *35*, 549-554.

45. Jang, Y. H.; Hwang, S.; Oh, J. J.; Joo, S.-W., Adsorption Change of Cyclohexyl Acetylene on Gold Nanoparticle Surfaces. *Vib. Spectrosc.* **2009,** *51*, 193-198.

46. Cai, M.; Mowery, M. D.; Pemberton, J. E.; Evans, C. E., Dual-wavelength Resonance Raman Spectroscopy of Polydiacetylene Monolayers on Au Surfaces. *Appl. Spectrosc.* **2000,** *54*, 31-38.

47. Moskovits, M., Surface Selection Rules. *J. Chem. Phys.* **1982,** *77*, 4408-4416.

48. Sheppard, N.; Erkelens, J., Vibrational Spectra of Species Adsorbed on Surfaces: Forms of Vibrations and Selection Rules for Regular Arrays of Adsorbed Species. *Appl. Spectrosc.* **1984,** *38*, 471-485.

49. Klingsporn, J. M.; Jiang, N.; Pozzi, E. A.; Sonntag, M. D.; Chulhai, D.; Seideman, T.; Jensen, L.; Hersam, M. C.; Duyne, R. P. V., Intramolecular Insight into Adsorbate–Substrate Interactions *via* Low-Temperature, Ultrahigh-Vacuum Tip-Enhanced Raman Spectroscopy. *J. Am. Chem. Soc.* **2014,** *136*, 3881-3887.

50. Zhong, J.-H.; Jin, X.; Meng, L.; Wang, X.; Su, H.-S.; Yang, Z.-L.; Williams, C. T.; Ren, B., Probing the Electronic and Catalytic Properties of a Bimetallic Surface with 3 nm Resolution. *Nat. Nanotechnol.* **2017,** *12*, 132-136.

51. Zhang, W.; Cui; Yeo, B.-S.; Schmid, T.; Hafner, C.; Zenobi, R., Nanoscale Roughness on Metal Surfaces Can Increase Tip-Enhanced Raman Scattering by an Order of Magnitude. *Nano Lett.* **2007,** *7*, 1401-1405.

52. Trautmann, S.; Aizpurua, J.; Gotz, I.; Undisz, A.; Dellith, J.; Schneidewind, H.; Rettenmayr, M.; Deckert, V., A Classical Description of Subnanometer Resolution by Atomic Features in Metallic Structures. *Nanoscale* **2017,** *9*, 391-401.

53. Chapman, M.; Mullen, M.; Novoa-Ortega, E.; Alhasani, M.; Elman, J. F.; Euler, W. B., Structural Evolution of Ultrathin Films of Rhodamine 6G on Glass. *J. Phys. Chem. C* **2016,** *120*, 8289-8297.

TOC Graphics